Journal of Materials Chemistry A

ROYAL SOCIETY OF CHEMISTRY

PAPER

View Article Online
View Journal | View Issue

Cite this: J. Mater. Chem. A, 2026, 14, 3071

Influence of europium ion doping on photoinduced properties of 2D cobalt hydroxide: photocatalytic degradation and negative photoconductivity studies

Viktorija Pankratova, [a] Rossella Greco, *[a] Takashi Yamamoto, [b] Joanna Hoszowska, [c] Meng Zhang, *[d] Ali M. Huerta-Flores, [e] Miikka Willman, [a] Kimmo Sirkka, [f] Vladimir Pankratov, [g] Rafal Sliz, [h] Yang Bai [f] and Wei Cao [a]

Transition metal hydroxides have been extensively used in the electrocatalytic oxygen evolution reaction; however, their use in photocatalytic processes remains less common. In this study, we report the successful synthesis of europium-doped (2.8 wt%) cobalt hydroxide nanoplates ($Co(OH)_2$:Eu) *via* one-pot hydrothermal synthesis for photocatalytic and photoconductive applications. The structural and electronic properties of europium-doped cobalt hydroxide were studied and compared with undoped $Co(OH)_2$ prepared *via* a similar procedure. $Co(OH)_2$:Eu exhibited increased stability compared to undoped $Co(OH)_2$. Potential applications of $Co(OH)_2$:Eu for photocatalytic pollutant degradation were evaluated on the basis of methylene blue degradation. The band structure of $Co(OH)_2$:Eu was proposed based on the photoconductivity behaviour. The mechanism of the driving forces of the photocatalytic degradation reaction was studied using band structure analysis and radical scavenger experiments. Furthermore, density functional theory (DFT) calculations provided a deeper understanding of the reason for the improved photocatalytic efficiency of $Co(OH)_2$:Eu. We established that $Co(OH)_2$:Eu possesses the local state above the conduction band edge, which induced a marked increase in the negative photoconductivity of $Co(OH)_2$:Eu due to the binding of electrons, highlighting the potential use of rare-earth doping in optoelectronic switches.

Received 8th September 2025
Accepted 26th November 2025

DOI: 10.1039/d5ta07316b

rsc.li/materials-a

Introduction

Photocatalytic reactions using renewable and infinite solar energy provide a sustainable approach within a fossil fuel-based economy. These processes include the use of a photocatalyst, which is usually a transition metal semiconductor. The use of photons to excite the semiconductor materials promotes the excitation of electrons from the valence band to the conduction band, leaving a positive hole in the valence band. The photoexcited electron and hole can behave as a redox pair and, after migration to the surface of the semiconductor, react with molecules adsorbed on the surface. Such photocatalytic reactions can be used to produce hydrogen and oxygen *via* water splitting and for wastewater treatment by oxidation of the pollutants in water. Currently, one of the environmental crises is the presence of pollutants in wastewater, such as pesticides, antibiotics, and other persistent pollutants, posing serious risks to human health and ecosystems due to their resistance to natural degradation. High energy consumption in current water treatment trends is the reason for the search for new methods.[1] Photocatalytic water treatment is considered a promising alternative due to its use of renewable solar energy as the power source.[2,3] Ideally, this approach does not require a lot of electricity, but only the energy coming from the sun would be sufficient. This is true in the case of highly efficient photocatalysts, which are still a subject under intense study due to some intrinsic drawbacks of these materials.

Common drawbacks of photocatalysts include charge–carrier recombination, poor stability, or wide bandgaps,[4–7] which can be improved through changes in crystallinity and dimensions, creating heterostructures, or doping.[8] An

[a]Nano and Molecular Systems Research Unit, University of Oulu, Oulu FIN-90014, Finland
[b]Department of Science and Technology, Tokushima University, Tokushima, 770 8506, Japan
[c]Department of Physics, University of Fribourg, Fribourg CH-1700, Switzerland
[d]School of Physics, East China University of Science and Technology, Shanghai 200237, China
[e]Research Unit of Sustainable Chemistry, University of Oulu, Oulu FIN-90014, Finland
[f]Microelectronics Research Unit, Faculty of Information Technology and Electrical Engineering, University of Oulu, Oulu FIN-90014, Finland
[g]Institute of Solid State Physics, University of Latvia, Riga LV-1063, Latvia
[h]Optoelectronics and Measurement Techniques Unit, University of Oulu, Oulu FIN-90014, Finland

appropriate bandgap (less than 3 eV) is necessary to ensure the electron–hole pair generation and thus photocatalytic activity under sunlight. Wide-bandgap semiconductors such as titania do not satisfy this requirement, as they require ultraviolet light irradiation for the reaction to be possible, while only 5% of the sunlight is in the ultraviolet region.[9–11] Crystal growth determines not only the phase of the synthesized material but also the size of the photocatalyst crystals and, consequently, the surface area, along with the number of active sites.[12] For example, dangling bonds at the surface of the materials are a great active site for chemisorption and, therefore, subsequent reaction at the surface.[9] Substitution with heteroatoms[13,14] and introduction of vacancies[15] into the structure are also among other surface defect creation methods for improved reactivity. Interestingly, the dimensions of the catalyst will even tune the bandgap of the material due to the surface plasmonic effect in smaller dimensionalities.[16] Two or more semiconductors joined together in a heterostructure prevent charge recombination, therefore limiting the processes competing with photocatalysis, such as radiative and nonradiative recombination. While also modifying the electronic structure, doping techniques act differently from the heterostructure production. Non-metal and transition metal doping have been widely used for increasing photocatalytic activity by enhancing the light absorbance in the visible light spectra.[17–21] Rare-earth doping of photocatalysts is also used for bandgap engineering and structure stabilization, inhibiting phase changes and stabilizing the material at increased temperatures.[22–24] Rare-earth metal introduction promotes the electron transfer of the reactive species and improve the redox properties of the host materials.[25,26]

Transition metals, specifically, nickel,[27–29] cobalt,[30–35] copper,[12,36–38] and iron,[39–42] are considered good options for producing photocatalysts, mainly because of their high abundance and low price, especially when compared to those of noble metals. Hydroxides of transition metals are known to be good photocatalyst matrices for the oxygen evolution reaction (OER), CO_2 reduction, and degradation of organic pollutants.[19,28,43,44] Furthermore, transition metal hydroxides were found to increase the yield of the hydrogen evolution reaction (HER) when modifying existing photocatalysts such as TiO_2, $ZnIn_2S_4$, and others.[29,45–48] Hence, the unique features of transition metal hydroxides are very much in demand to mitigate climate, energy and water crises.

Cobalt hydroxide has been previously identified as an electrocatalyst and photocatalyst for the OER.[31,33,49–53] On the other hand, the basicity of the hydroxyl groups makes the adsorption of water at the surface challenging, which significantly affects the water splitting to obtain hydrogen.[54] Doping cobalt hydroxide with rare-earth metals can improve its photocatalytic activity by increasing its internal resistance and favouring the charge transfer at the surface, a crucial factor in any photocatalytic applications.[55] Furthermore, cobalt hydroxide has been proven to be unstable by itself under irradiation, and only the presence of secondary species could avoid this undesired event.[30]

The study of photoexcited charge carriers and their behaviour is possible by monitoring the photoconductivity of the semiconductor, or the change in electrical conductivity upon light illumination. The cause of the conductivity change is the creation of electron–hole pairs under photoexcitation, the initial step being the same as in photocatalysis. Depending on how the photo-excited charge carriers migrate, the photoconductivity may increase or decrease, and this phenomenon constitutes the basis of several applications of semiconductors, such as photoresistors and photodetectors.

Negative photoconductivity, where the conductivity of the material decreases under illumination, is less commonly observed than positive photoconductivity. This process is attributed to charge carrier trapping. For example, in low-dimensional materials, trap centres and numerous surface defects are responsible for trapping electrons, causing the charge carrier flow and subsequently the conductivity to decrease.[56,57] The applications of semiconductors with negative photoconductive properties include optoelectronic sensors, optical memory devices, optical switches, and more.[58–60] To date, the photoconductivity of $Co(OH)_2$ has not been well studied, as previous research has focused more on layered hydroxides[61] or other cobalt-containing semiconductors[62,63] that are typically used as photocatalysts. Indeed, photoconductivity studies complement the search for the semiconductors that would be ideal for photocatalytic applications and help to understand the behaviour of charge carriers.[64]

In this work, we report a novel approach to enhance the structural and functional properties of β-$Co(OH)_2$ by doping it with Eu^{3+}. The introduction of Eu ions into the $Co(OH)_2$ lattice significantly improves the material's thermal stability, as demonstrated by thermogravimetric analysis. Importantly, the photocatalytic activity of $Co(OH)_2$ is preserved, as is demonstrated through methylene blue degradation experiments as a proof of concept. Computational studies confirmed the findings obtained by photocatalytic degradation, observing an easier desorption of radicals responsible for the reaction from the europium-doped $Co(OH)_2$. Exceptionally, by photoconductivity measurements, we could demonstrate the europium-doped material to exhibit an enhanced negative photoconductivity response, which could open its application as an optoelectronic detector or switch.[60] Overall, we open the path for a new family of materials, such as rare-earth doped transition metals hydroxides, to be applied in photomediated processes.

Experimental methods

Synthesis

The synthesis was carried out in a similar manner as previously reported by our research group.[30] Cobalt nitrate hexahydrate ($Co(NO_3)_2 \cdot 6H_2O$, ≥98.0%, Sigma-Aldrich), polyethylene glycol-6000 ($H(OCH_2CH_2)_nOH$, Alfa Aesar), europium nitrate hydrate ($Eu(NO_3)_3 \cdot H_2O$, 99.99%, Sigma-Aldrich), absolute ethanol (99.5%, ETAX), and deionized water were used. All reactants were used without any further purification. 0.5 mmol of $Co(NO_3)_2 \cdot 6H_2O$ and 0.5 g of polyethylene glycol-6000 (PEG-6000) were stirred in 20 mL of H_2O at 500 rpm for 30 min. The necessary volume of 3 mM $Eu(NO_3)_3$ aqueous solution was then added dropwise to the stirring reaction mixture to reach

the nominal 3 wt% of europium. The aqueous solution of NaOH (10 w/v%) was added dropwise until the pH reached 12. Subsequently, the solution was stirred for 10 minutes and transferred to a 40 mL Teflon-lined stainless-steel autoclave. The autoclave was heated at 180 °C for 24 hours for the hydrothermal reaction to occur and then the autoclave was naturally cooled down to room temperature. The mixture with the precipitate was transferred to a centrifuge tube and was centrifuged at 4000 rpm for 15 min and then washed twice with water and ethanol at 4000 rpm for 15 min. The pink color precipitate was dried under vacuum overnight.

Characterization

The phase content of the synthesized samples was confirmed by powder X-ray diffractometry (XRD). Powder XRD measurements were performed utilizing a Rigaku SmartLab 9 kW system using Co Kα radiation (λ = 1.79 Å, 40 kV, 135 mA) and a Rigaku MiniFlex 600 using Cu Kα radiation (λ = 1.54 Å, 40 kV, 15 mA). Europium content was determined using inductively coupled plasma-optical emission spectroscopy (ICP-OES), Agilent 5110 VDV (Agilent Technologies Inc., Santa Clara, California, USA). Prior to the analysis, 6.2 mg of $Co(OH)_2$:Eu were dissolved in approximately 1 mL of aqua regia and diluted with deionized water until the total volume was 5 mL. Differential scanning calorimetry-thermogravimetry (DSC-TG) measurements were performed using a Netzsch STA 409 in the temperature range of 38–803 °C in the air with a rate of 10 K min^{-1}.

Scanning electron microscopy (SEM) images were obtained using a Zeiss Sigma FESEM (field emission scanning electron microscope). The samples were suspended in ethanol and the suspensions were dried on a silicon wafer prior to the experiment. Transmission electron microscopy (TEM) images were taken using a JEOL JEM-2200FS EFTEM/STEM (energy filtered transmission electron microscopy/scanning transmission electron microscopy) setup. The suspensions of the samples in ethanol were applied dropwise on the C/Cu TEM grids and dried. X-ray photoelectron spectroscopy (XPS) measurements were performed employing an ESCALAB 250Xi using Al Kα radiation and a Au grid.

Electrochemical impedance spectroscopy (EIS) was conducted using a Metrohm Vionic electrochemical station (Metrohm). The frequency range was set from 5 MHz to 0.01 Hz with an amplitude of 10 mV. The measurements were performed at room temperature. Fitting of the Nyquist plot was performed on data recorded at −0.3 V *vs.* Ag/AgCl under illumination across a frequency spectrum ranging from 0.1 Hz to 1 MHz using a potentiostat–galvanostat (Corrtest Instruments Model CS310M) with EIS capabilities.

Diffuse reflectance spectra of the undoped and doped powders in the ultraviolet-visible (UV-Vis) region were measured using a Shimadzu UV-2600 spectrophotometer using the diffuse reflectance of $BaSO_4$ (Nacalai Tesque Inc.) as a reference.

Kelvin probe force microscopy (KPFM) images were recorded using a NanoSurf FlexAFM system equipped with a C3000i Controller (Nanosurf AG, Switzerland). The work function of the Multi75-G tip was calibrated using highly oriented pyrolytic graphite (HOPG) on a support (Nanosurf AG). Image analysis was performed using the Gwyddion software.[65] The sample was prepared *via* drying the sample suspension in ethanol on a Si wafer.

Commercially produced $Co(OH)_2$ nanoplates (FUJIFILM Wako Pure Chemical Corporation) were used for comparison.

X-ray absorption spectroscopy study

X-ray absorption spectra were recorded with a laboratory-type spectrometer R-XAS Looper[66] (Rigaku) in transmission mode at the Co K- and Eu L_3-edge. Curved monochromator crystals Ge(220) and Si(400) were used for extended X-ray absorption fine structure (EXAFS) and X-ray absorption near edge structure (XANES) experiments, respectively. The data reduction was performed with the REX2000 program.[67] The radial structure function (RSF) was obtained by Fourier transformation of k^3-weighted EXAFS in the range of *ca.* 2–9 $Å^{-1}$. Note that the available *k*-range for $Co(OH)_2$:Eu samples at the Co K-edge is restricted up to *ca.* 9.5 $Å^{-1}$ due to interference of the Eu L_1 edge. The phase shift and backscattering amplitudes were calculated using the FEFF8.4 program.[68] The lab-based XAS spectrometer was selected so that the radiation damage of the hydroxides[30] can be avoided.

Photoluminescence

Photoluminescent properties of the materials were studied under synchrotron radiation excitation. The experiments were carried out at the Superlumi setup installed at the P66 beamline of the PETRA III storage ring at the DESY synchrotron (Hamburg, Germany). The details of the setup can be found elsewhere.[69,70] The experiments were carried out under ultra-high vacuum conditions at 12 K. The emission spectra were measured under excitation with 4.1 eV photons.

Methylene blue degradation

Methylene blue (MB) dye was purchased from Sigma-Aldrich. The photocatalytic activity of the studied samples was evaluated by testing the photocatalytic methylene blue degradation under white-light LED illumination (0.495 W), which was provided by a PerfectLight PCX50B photoreactor. All experiments were carried out in glass reactors with quartz bottoms. During the photocatalytic experiment, 5.5 mg of the catalyst was added to 25 mL of solution containing 5 mL of 50 mg L^{-1} MB and 20 mL of deionized water, leading to a final MB concentration of 10 mg L^{-1}. The amount of the catalyst used was chosen to be similar to that reported elsewhere.[27,30] At given time intervals, the solutions were filtered through 0.22 μm filters (Electron Microscopy Sciences). The MB degradation behaviour was monitored by observing the changes in the absorbance of the solution in the visible range using a Shimadzu UV-2600 spectrophotometer (λ = 665 nm). The photolysis reaction of MB was conducted under similar conditions, omitting only the catalyst. The effect of adsorption was studied by stirring the MB solution with the added catalyst in the dark and observing the changes in absorbance in the same way.

The mechanism of the photocatalytic degradation reaction of MB was studied by adding 20 μL of isopropanol (Sigma-

Aldrich) to the initial solutions to assess the role of $OH^{\bullet}$ radicals. The degradation of MB was observed *via* HPLC using a Shimadzu Prominence LC system with a fluorescence detector ($\lambda = 290$ nm). The chromatographic separation was performed using an ACQUITY UPLC® BEH C18 1.7 μm column (2.1 mm × 100 mm). 0.1% formic acid aqueous solution and 0.1% formic acid solution in acetonitrile were used as a mobile phase with a flow rate of 0.9 mL min^{-1} and a composition of 15% of 0.01% formic acid in acetonitrile, which increased to 85% for the first 8 minutes, was held at 85% for one minute and then decreased back to 15% for the last 2 minutes.

To assess the role of oxygen in the photocatalytic degradation reaction, the reaction system was purged for 30 minutes with argon. The photocatalytic activity of $Co(OH)_2$:Eu was also studied in basic media (pH 9), which was adjusted with 10 wt% NaOH solution. Finally, the photocatalytic degradation of other concentrations of MB was also studied (5 and 15 mg L^{-1}). The reaction was monitored by observing the absorbance changes as mentioned above.

Photoelectrochemical characterization

Electrodes composed of active materials ($Co(OH)_2$ and $Co(OH)_2$:Eu) were prepared through the following procedure: 5 mg of the powder materials was dispersed in 500 μL of absolute ethanol along with 0.5 μL of ethanolamine. This mixture was subjected to ultrasonic treatment for 5 minutes. Subsequently, 0.1 mL of the resulting solution was deposited onto a fluorine-doped tin oxide (FTO) conductive substrate and spin-coated at a rotation speed of 2000 rpm for 45 seconds. The film was then dried at 80 °C for 30 min. An electrical connection to the film was established using a copper wire and silver paint, with the active area of the film measured to be 1 cm^2.

Photoelectrochemical tests were conducted in a quartz cell utilizing a potentiostat–galvanostat (Corrtest Instruments Model CS310M) with EIS capabilities. The electrodes containing photoactive material served as the working electrode, while a platinum wire acted as the counter electrode and a silver/silver chloride (Ag/AgCl) electrode functioned as the reference electrode. A 0.1 M sodium sulfate (Na_2SO_4) solution (pH 7) was employed as the electrolyte. Illumination of the electrodes was achieved from the front side using a UV-Vis lamp with a measured spectral irradiance of 1109.21 W m^{-2}. Chronoamperometric tests were carried out over a duration of 100 seconds at an applied potential of 0.3 V *vs.* Ag/AgCl, with the light shutter being opened and closed every 10 seconds. Mott–Schottky plots were generated at a frequency of 500 Hz across a potential range of 0.3 to −1 V *vs.* Ag/AgCl.

To convert the flat band potential values measured electrochemically to energy in eV *vs.* vacuum, the following eqn (1) was used, where 4.645 eV is the absolute potential of the Ag/AgCl (3.5 M KCl) reference electrode with respect to the vacuum energy level.[71]

$$E_{(\mathrm{eV}\ vs.\mathrm{vacuum})} = -\left(E_{\left(\mathrm{V}\ vs.\ \frac{\mathrm{Ag}}{\mathrm{AgCl}}\right)} + 4.645\right) \quad (1)$$

Photoconductivity measurements

Interdigitated Au electrodes were first deposited on a glass substrate *via* sputtering. 25 mg of $Co(OH)_2$ and $Co(OH)_2$:Eu were suspended individually in 2.5 mL of ethanol (96% v/v). The suspensions were then drop-casted onto the substrates with electrodes and dried at 80 °C on a hot plate. Current–voltage (*I*–*V*) curve measurements were performed at room temperature using a source measure unit (2450, Keithley, USA). The samples were measured in a dark room without illumination and under the illumination of lasers (Coherent Inc., USA) operating at 20 mW. The nominal wavelengths of the lasers were 660 nm, 552 nm, and 405 nm, corresponding to photon energies of 1.88 eV, 2.25 eV, and 3.06 eV, respectively. Homogeneity of the sample coverage on the electrodes and the elemental composition were evaluated using a Zeiss ULTRA plus FESEM equipped with an EDS (energy dispersive X-ray spectroscopy) detector. The samples were coated with carbon prior to the FESEM and EDS analyses.

Computational methods

The computational work was executed by employing the first-principles approach incorporated in the Vienna *Ab initio* Simulation Package (VASP).[72] In the process of geometry optimization, the Perdew–Burke–Ernzerhof (PBE) functional, which falls under the category of the Generalized Gradient Approximation (GGA), was harnessed to depict the exchange–correlation interactions among electrons.[73,74] A plane-wave cutoff energy of 400 eV was established, and the Brillouin zone (BZ) was sampled utilizing a 2 × 2 × 1 *k*-point grid in accordance with the Monkhorst–Pack scheme.[75] The convergence criteria were determined as 10^{-5} eV for the total energy and 0.02 eV $Å^{-1}$ for atomic forces. To take into consideration the van der Waals interactions, the DFT-D3 correction method was put into effect.[76] In addition, a vacuum layer measuring 20 Å along the *z*-axis was incorporated with the aim of eliminating periodic interactions. The DFT + *U* method was employed to characterize the localized Eu 4f and Co 3d states, with U values of 7 eV and 4.5 eV, respectively.

Results and discussion

The successful synthesis of the β-cobalt hydroxide was proved by XRD (Fig. 1a). The visible peaks can be indexed to the (001), (100), (101), (002), (102), (110), (003), (200), (103), (021), and (112) planes of β-$Co(OH)_2$ (ICDD card number 00-045-0031). Minor Co_3O_4 peaks that can be attributed to the (311) and (440) planes can be observed in the spectra, as cobalt hydroxide is metastable and tends to convert to cobalt oxide.[30,77] In contrast, separate europium compound signals are not present, signifying the inclusion of europium in the structure of cobalt hydroxide and the absence of bigger Eu-based aggregates, such as nanoparticles. The cobalt hydroxide peaks show a uniform 0.3° shift to the higher angle values, reflecting the increase in the interplanar distance after the inclusion of Eu ions with a larger radius. The changes in the lattice parameters after Eu

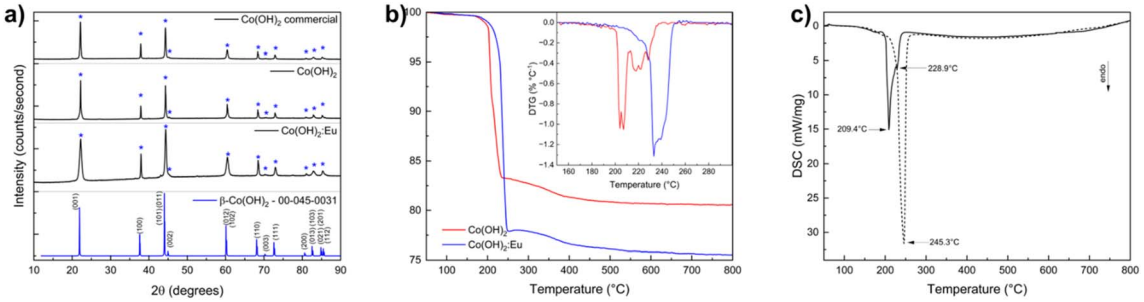

Fig. 1 Measured XRD patterns (a) of $Co(OH)_2$, $Co(OH)_2$:Eu and commercial $Co(OH)_2$ (in black), and simulated XRD reflections of β-$Co(OH)_2$ (in blue); thermogravimetric analysis (b) and differential scanning calorimetry curves (c) of pure and doped $Co(OH)_2$. The inset shows the derivative of the thermogravimetric curve.

doping are shown in Table S1. As expected, doping with a larger ion results in an increase in the crystal parameters. The europium content in $Co(OH)_2$:Eu, 2.8 wt%, was determined by ICP-OES, underlining that all the nominal Eu was introduced into the $Co(OH)_2$ structure.

In order to first distinguish between the two materials, the stability of the synthesized materials was analyzed using the DSC-TG method (Fig. 1b and c) and compared with each other. The derivative of the thermogravimetric curve is shown for clearer analysis (Fig. 1b, inset). It can be observed that the thermal behaviour of both samples can be categorized into similar stages. The mass of both pure and doped $Co(OH)_2$ gradually decreases by less than one percent until 150 °C due to dehydration and loss of absorbed water molecules. Further thermal degradation of pure $Co(OH)_2$, that is, 16.7% of weight loss after the main reaction at 210 °C, occurred following the pathway of transformation through CoOOH to Co_3O_4, as already described in the literature.[78–80] It is worth noting that the thermal degradation of $Co(OH)_2$:Eu is similar; however, the above-mentioned transitions happened at 20 °C higher than the corresponding temperature for the undoped hydroxide. Additionally, both the thermogravimetry (Fig. 1b) and differential scanning calorimetry (Fig. 1c) results show that $Co(OH)_2$:Eu exhibits fewer phase transitions, signified by the lack of peak shoulders. After heating the materials at 250 °C and 450 °C, XRD was performed (Fig. S1) to confirm the better thermal stability of $Co(OH)_2$:Eu compared to $Co(OH)_2$. Indeed, at 450 °C both materials transform into Co_3O_4. However, after heating at 250 °C, a clear difference between the hydroxide and the doped material is evident – while $Co(OH)_2$ after thermal degradation has transformed into Co_3O_4 and CoOOH completely, thermally degraded $Co(OH)_2$:Eu still contains a significant amount of β-$Co(OH)_2$ according to the quantitative XRD analysis. This leads to the conclusion that europium ions are stabilizing the β-$Co(OH)_2$ structure by delaying its conversion to CoOOH or Co_3O_4, which are less efficient materials in photocatalysis due to the low electrical conductivity and the unexceptional dimensionality.[55] It is important to note that at both studied temperatures, the XRD spectra of $Co(OH)_2$:Eu exhibited unidentified peaks, which we suppose are associated with a europium-containing phase.

To confirm the presence of Eu and to prove the even element distribution in the sample, the materials' morphology was examined using TEM coupled with EDS and SEM. Fig. 2 shows the distribution of the elements across the as-synthesized material obtained by EDS mapping. Europium was found to be distributed across the whole surface of the cobalt hydroxide nanoplates, and no europium agglomeration was detected, in line with the observation on the XRD pattern. However, the elemental mapping showed a higher europium signal at the edges of the particles. Additional SEM images can be found in the SI (Fig. S2). The STEM (Fig. 2a–d) and TEM (Fig. 2e) images showed a deviation from a typical hexagonal morphology of the pristine cobalt hydroxide (Fig. S2). Although the particles still possess the two-dimensional structure previously reported,[20,79,81] the edges of the nanoplates appear rounded and less regular. The two-dimensional sheets are approximately 100–150 nm in width and ~10 nm in thickness, as determined by HRTEM in Fig. 2f, with a similar size distribution shown in Fig. S3.

The SAED (selected area electron diffraction) pattern (Fig. 2g) agrees with the XRD pattern and shows a predominant $Co(OH)_2$ phase. No separate europium-containing compound was detected. The shadows near the $Co(OH)_2$ signals correspond to continuously growing Co_3O_4 formed under the electron beam, which enhances the oxidation process.[77]

Furthermore, the chemical environment of $Co(OH)_2$:Eu was studied using XPS, which revealed additional information about the changes induced by doping. The XPS survey (Fig. 3a) shows cobalt, oxygen, and europium as the main elements of the material. The indium 3d signal in the survey is associated with the sample holder used. In the Co 2p spectrum (Fig. 3b), Co $2p_{3/2}$ peaks at 780.9 eV and 783.0 eV are associated with Co^{2+} ions, which is consistent with the nature of $Co(OH)_2$. A low-intensity shoulder at 777.7 eV, usually attributed to metallic cobalt, appears due to metal formation on the surface of the sample after reduction by the probe beam.[82] Co $2p_{1/2}$ peaks at 795.9 eV and 796.9 eV are also present and arise from spin–orbit coupling. Additionally, shake-up satellite peaks are present in the Co 2p spectrum. The cobalt peaks show a small shift to lower energies when compared to pristine $Co(OH)_2$ in the literature[83] as well as $Co(OH)_2$ synthesized using the same method. The positive shift in the values of the cobalt peaks

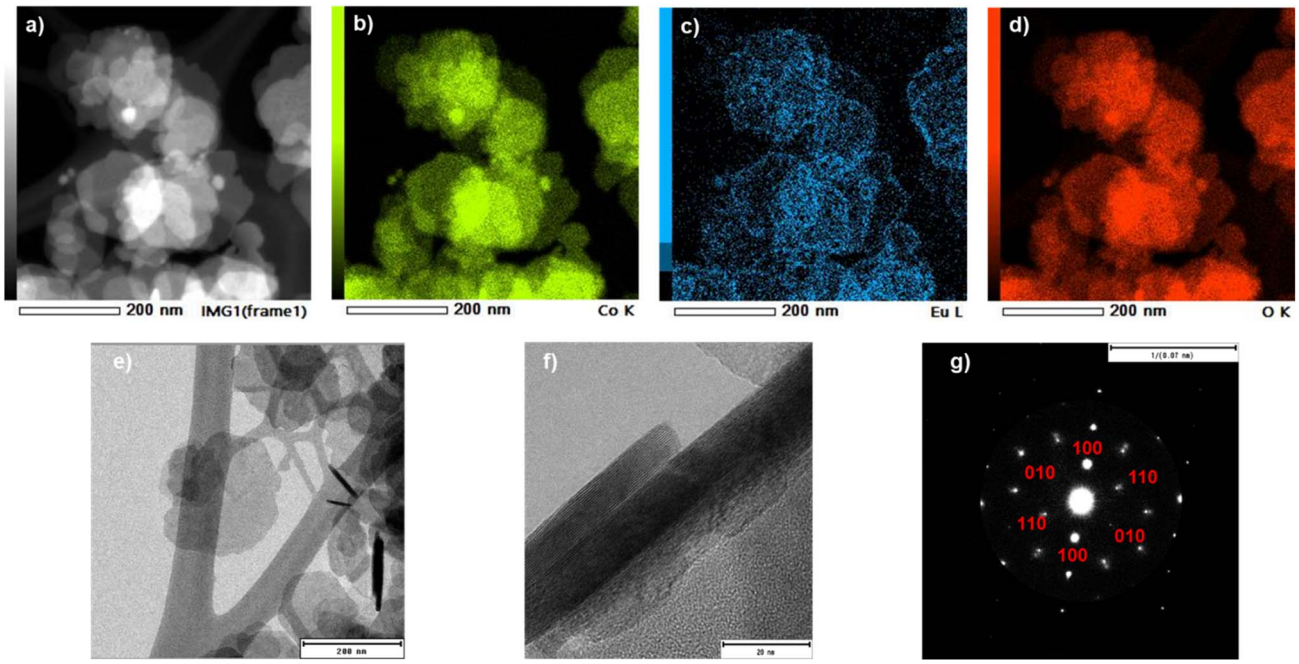

Fig. 2 STEM image of the $Co(OH)_2$:Eu nanoparticles (a) and elemental mapping of Co (b), Eu (c), and O (d); TEM image (e) and side-view HR-TEM (high-resolution TEM) image of a $Co(OH)_2$:Eu particle (f); and SAED pattern of $Co(OH)_2$:Eu (g).

(Table S2) is consistent with doping with europium – an element with a lower electronegativity than cobalt. This results in an increase in the electron density around cobalt and a subsequent decrease in cobalt binding energy. The Eu 3d spectrum (Fig. 3c) shows spin–orbit coupling into Eu $3d_{5/2}$ and $3d_{3/2}$ peaks, as well as a shake-up satellite and two shake-down

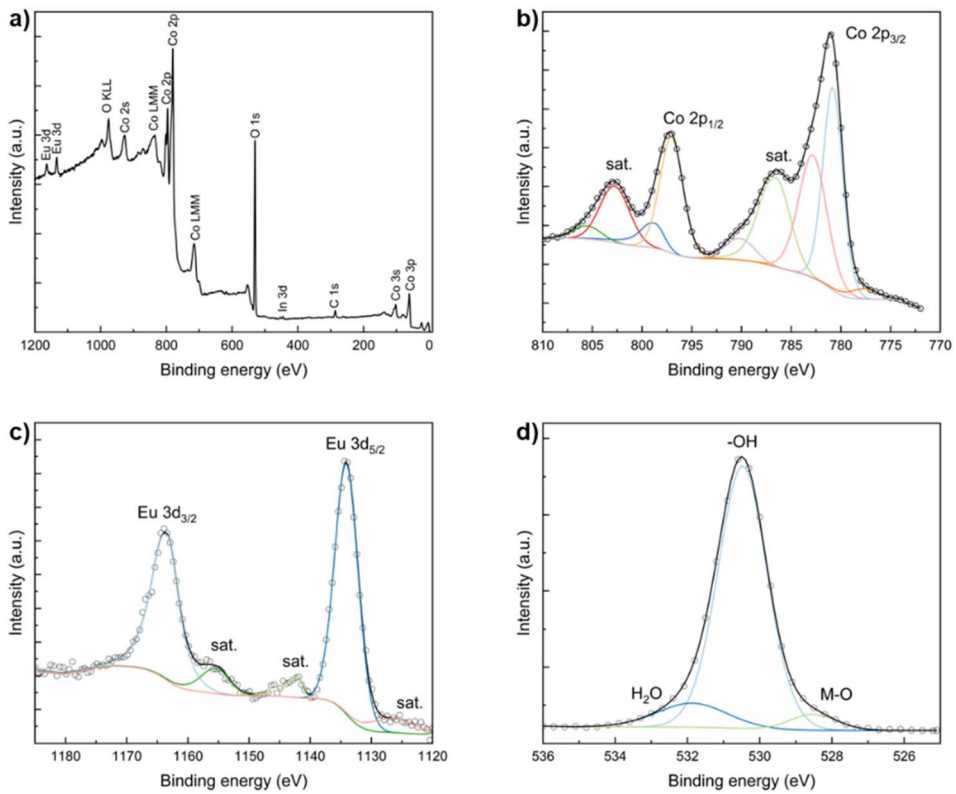

Fig. 3 XPS survey of $Co(OH)_2$:Eu (a) and XPS spectra of Co 2p (b), Eu 3d (c), and O 1s (d). The experimental data are shown as circles and the fitted data are shown as solid lines.

satellites. The corresponding energies of these peaks are 1135.0 eV and 1164.6 eV, respectively, which are typical for Eu^{3+}, and no shifts in binding energy are observed compared to the values in Eu_2O_3 (ref. 84) (Table S2). The O 1s spectrum (Fig. 3d) shows three peaks and mainly consists of the XPS peak with the energy of 530.5 eV. It is associated with the oxygen that is bonded to hydrogen, *i.e.*, the hydroxide group (O–H). The higher energy peak at 531.9 eV is typically assigned to the oxygen in the adsorbed water molecules. The peak at 528.5 eV is attributed to the metal–oxygen (M–O) bond in the lattice.[85]

The chemical state and the local structure of the synthesized $Co(OH)_2$:Eu nanoplates were studied using in-house X-ray absorption near-edge structure (XANES) and extended X-ray absorption fine structure spectroscopy (Fig. 4). The Co K-edge XANES (Fig. 4a) experiments were performed, and the results of the synthesized europium-doped cobalt hydroxide were compared with the commercially available reference compounds, $Co(OH)_2$ and CoO (Wako Pure Chemical Industries, Ltd). The absorption edge of $Co(OH)_2$:Eu is the same as that of $Co(OH)_2$, indicating that the Co species is divalent. This is consistent with the XPS results discussed above. The Eu L_3-edge XANES (Fig. 4b) experiments were performed and compared with Eu_2O_3 and EuS to confirm the existence of Eu^{3+} species in the synthesized cobalt hydroxide. Strong intensity of the "white line" peak of the Eu L_3-edge is caused by the difference in the amount of unoccupied Eu 5d states compared to Eu_2O_3. Further data analysis and calculations were performed using the Co K-edge XANES spectra to get more insights into the sample structure.

Fig. 4c depicts the EXAFS spectra. The Fourier transforms of the Co K-edge EXAFS oscillations, shown in Fig. 4d, establish the similarity of the structure of the synthesized europium-doped cobalt hydroxide to that of an undoped commercial powder and show the absence of a relevant amount of cobalt oxides. The EXAFS parameters summarized in Table S3 support this proposal by confirming similar Co–O coordination numbers in $Co(OH)_2$ and $Co(OH)_2$:Eu, but different ones in the case of Co–Co.

Computational geometry optimization provides more insight into the structural changes occurring in $Co(OH)_2$ upon doping with europium. Fig. 5a and b present the geometrically optimized unit cells of β-$Co(OH)_2$ and $Co(OH)_2$:Eu, respectively. The β-$Co(OH)_2$ unit cell crystallizes in the hexagonal system with space group $P\bar{3}m1$. In this structure, all Co atoms are six-coordinated, forming a hexagonal arrangement with O atoms. The lattice constants are determined as $a = b = 3.18$ Å, $c = 3.62$ Å, $\alpha = \beta = 90°$, $\gamma = 120°$, consistent with previous studies.[86,87] Notably, prior research has demonstrated that the (001) facet of β-$Co(OH)_2$ exhibits lower surface energy,[88] which justifies our focus on this specific facet for subsequent investigations. Upon Eu doping in $Co(OH)_2$:Eu, structural changes emerge, *i.e.*, the Eu–O bond length increases to 2.37 Å, significantly longer than the Co–O bond length of 2.04 Å. Furthermore, the bond angles involving Eu–O and O–H show a marked enlargement compared to the undoped system. These modifications highlight the lattice distortion induced by Eu incorporation, which may influence the material's electronic and catalytic properties.

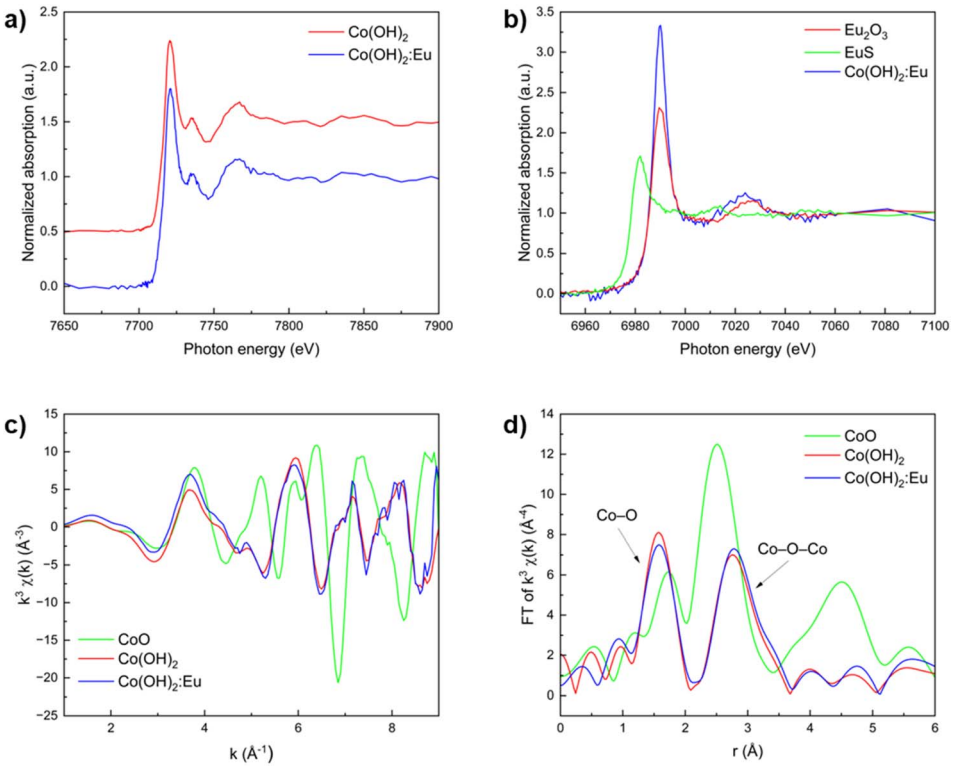

Fig. 4 Co K-edge (a) and Eu L_3-edge (b) XANES spectra, Co K-edge EXAFS spectra (c), and Fourier transforms (d) of the synthesized $Co(OH)_2$:Eu and the commercially produced $Co(OH)_2$ and CoO samples.

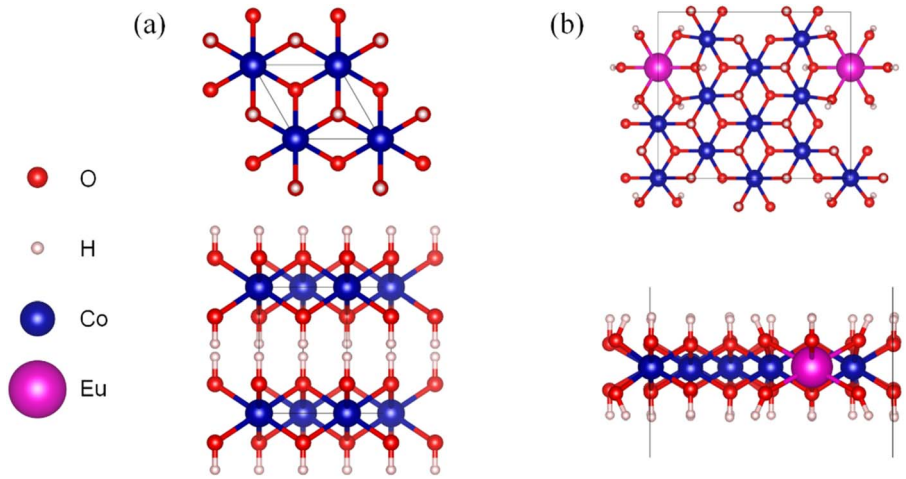

Fig. 5 Top view (upper) and side view (lower) of β-$Co(OH)_2$ (a) and $Co(OH)_2$:Eu (b), with one Eu atom displayed as a periodic mirror image.

After establishing the elemental and structural composition of the synthesized samples, we studied the electrical and optical properties of $Co(OH)_2$:Eu in order to confirm its applicability in photocatalysis, as well as its interaction with light in the ultraviolet and visible range. Diffuse reflectance spectra (Fig. 6a) reveal the absorption of Co^{2+} ions in the octahedral crystal field and contain the band characteristic of the $^4T_{1g}(F)$–$^4T_{1g}(P)$ (υ_3) transition at around 530 nm.[89,90] High absorption of both doped and undoped samples in the ultraviolet region has been associated with the ligand-to-metal charge transfer (LMCT) process. The diffuse reflectance spectra were then transformed into the Kubelka–Munk function using eqn (2):

$$(\hbar\nu F(R_\infty))^2 = A(\hbar\nu - E_g) \quad (2)$$

The data were then analysed using the Tauc equation to determine the bandgap of the materials. The resulting Tauc plot and fitting are shown in Fig. S4, illustrating a nominal bandgap of 2.05 eV in Eu-doped $Co(OH)_2$ (Fig. S4a), as opposed to 2.17 eV in undoped $Co(OH)_2$ synthesized using the same method (Fig. S4b) and approximately 1.8–1.9 eV for β-$Co(OH)_2$ synthesized using other methods.[30,91–93] These values are not far off from the density functional theory calculations of the band structure of monolayer $Co(OH)_2$ (1.52 eV)[94] and bulk $Co(OH)_2$ (2.00 eV).[95] The decrease in the bandgap after doping confirms the inclusion of the europium ions in the lattice and their displacement of Co^{2+} ions. The XPS valence band spectra (Fig. S4c), calibrated at the O 2s peak value, were used to determine the value of the valence band of the material

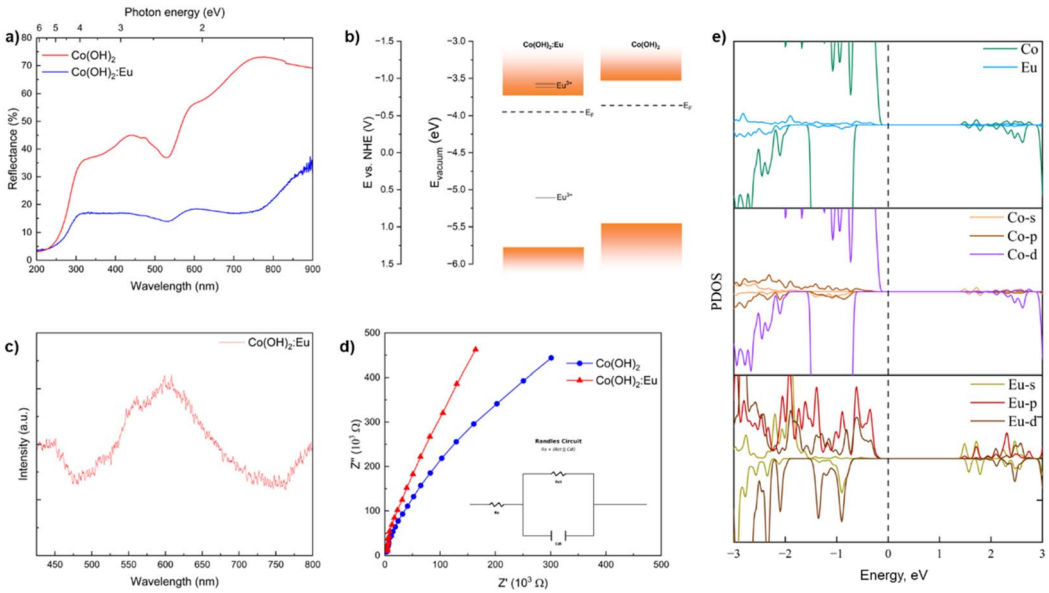

Fig. 6 Diffuse reflectance spectra of undoped and Eu-doped $Co(OH)_2$ (a), proposed band structure of $Co(OH)_2$:Eu in comparison with that of undoped $Co(OH)_2$ (ref. 30) (b), luminescence spectra of $Co(OH)_2$:Eu at 12 K (luminescence excitation 4.1 eV) (c), Nyquist plots of $Co(OH)_2$ and $Co(OH)_2$:Eu (d), and the PDOS (partial density of states) of Eu and Co atoms, and their s, p, and d states in $Co(OH)_2$:Eu (e).

(−5.78 eV *vs.* vacuum). The lowest energy of the conduction band was then calculated based on the known valence band and the bandgap energies, which −3.73 eV. The Fermi level of the doped hydroxide was calculated based on the contact potential difference from the KPFM images (Fig. S5), which turned out to be −3.95 eV. The latter value confirms the doped material as a negative semiconductor, as is the case for undoped $Co(OH)_2$. Both the valence and the conduction band values (Fig. 6b) show a slight change compared to undoped $Co(OH)_2$ introduced by the inclusion of Eu^{3+} in the structure. Indeed, doping with transition and rare-earth metal ions is a well-known bandgap engineering method.[96,97] In heavily doped semiconductors, the density of states changes with the introduction of the dopants, slightly changing the positions of the valence band maximum and the conduction band minimum. When the dopant states interact with each other, they form the impurity band around the dopant energy levels. The broadening of the dopant band and the formation of the band tails may cause bandgap narrowing and valence band shift towards the majority carrier band.[98,99]

Photocatalysis and photoluminescence are competing processes, resulting from different behaviours of photo-excited electrons and holes. For photocatalysis, reactions occur at the surface of the material, while for photoluminescence, radiative recombination occurs inside the material. Therefore, we performed photoluminescence experiments to study the relaxation mechanism after the excitation. Cobalt-containing compounds are connected to low luminescence intensity, and thus cobalt is considered a luminescence "killer" along with iron and nickel.[100,101] Luminescence quenching properties of cobalt are apparent even when present in the structure with a low doping concentration. The photoluminescence spectra of europium-doped cobalt hydroxide (Fig. 6c) show a broad and shapeless luminescence band in the yellow region of the spectra, but the undoped cobalt hydroxide was not found to emit light. The lack of photoluminescence of undoped $Co(OH)_2$ signifies that no radiative recombination takes place. The shape of the luminescence band of $Co(OH)_2$:Eu is a characteristic of surface defect radiative recombination in nanoparticles. However, the spectra of the doped $Co(OH)_2$ lack the characteristic Eu^{3+} f–f lines at 580–620 nm of high intensity.[102–104] The shape of the spectra, along with the established presence of Eu^{3+} ions proven by XPS and XAS, provides the possibility that the excited electron level of europium is located well above the bottom of the conduction band. Indeed, for the radiative recombination to successfully occur, both ground and excited 4f electron levels of Eu^{3+} should be located inside the bandgap, which is utilized in europium-doped luminophores such as titania, molybdates, phosphates, vanadates, and many others.[102,103,105–109] While the energy difference between the ground and excited levels varies among different compounds where the lanthanides act as the dopants, in the case of Eu^{3+}, it is larger than the determined bandgap of $Co(OH)_2$.[110,111] This explains different optical and luminescence properties than expected from materials doped with trivalent europium ions. Therefore, we can assume that a similar process of non-radiative recombination occurs in $Co(OH)_2$, possibly through the existence of deep levels in the bandgap acting as traps. The influence of different energy levels in the doped and undoped $Co(OH)_2$ is further explained below in relation to photoconductivity.

Even though the inclusion of trivalent europium in the material does not cause the radiative 4f–4f recombination, it does include more unfilled levels into the conduction band of the material (Fig. 6b), possibly contributing to the creation of the superoxide radical $O_2^{-\bullet}$ (ref. 112) that is responsible for the photocatalytic degradation of organic compounds after transformation to $OH^{\bullet}$.[113]

To confirm our hypothesis regarding the band structure of the materials, we used DFT calculations. As shown in Fig. 6e, the introduction of trivalent Eu incorporates more unfilled energy levels into the conduction band of the material, altering its electronic structure and increasing the density of electronic states in the conduction band. We primarily considered the energy level contributions of Co and Eu to $Co(OH)_2$:Eu. The valence band top of $Co(OH)_2$:Eu is mainly contributed by the d orbitals of Co and the p and d orbitals of Eu, while the conduction band bottom is primarily contributed by the s orbitals of Co and Eu. Due to the self-interaction errors in the strongly localized orbitals, f-elements are notoriously difficult to describe with DFT. Therefore, it is regrettable that the contribution of the Eu 4f orbitals was not considered in this analysis of atomic orbital contributions. However, the Eu 4f contribution can be visualized in the photoconductivity analysis discussed below.

Electrochemical impedance spectroscopy (Fig. 6d) was used to determine the ionic conductivity changes in $Co(OH)_2$ upon doping with europium. The ionic conductivities derived from EIS are 1.61×10^{-8} S cm^{-1} for pure $Co(OH)_2$ and 3.98×10^{-9} S cm^{-1} for europium-doped $Co(OH)_2$. Higher ionic conductivity and a smaller semicircle in the Nyquist plot (Fig. S6, with the Randles circuit model fitting results in Table S4) in the case of undoped hydroxide signify a lower charge transfer resistance (R_{ct}) and a more effective charge carrier separation, and, as a result, a lower degree of recombination processes. The R_{ct} parameter relates to the facility of the photogenerated charges to reach the electrolyte. In $Co(OH)_2$:Eu, the larger R_{ct} values imply a more complex interfacial charge transfer kinetics, due to charge trapping induced by Eu^{3+} doping. These trap sites temporarily hold photogenerated charges and reduce recombination, promoting a higher photocurrent. From the point of view of the EIS measurements, the undoped hydroxide would be a better photocatalyst than the doped one. This seems to confirm the previously described defect-related luminescence of $Co(OH)_2$:Eu compared to the lack of luminescence in the case of pure $Co(OH)_2$.

The band structures examined above are clearly reflected by the photoconductivity results. Fig. 7a shows an example of such results for Eu-doped $Co(OH)_2$. It can be seen that as the photon energy increased, the same electric field induced a smaller current density, indicating negative photoconductivity. In fact, negative photoconductivity is observed in both undoped and doped $Co(OH)_2$, as shown in Fig. 7b, but the evolution of conductivity as a function of incident photon energy experienced a bifurcation after 2.25 eV. The decrease in conductivity

stopped at an incident photon energy of 2.25 eV for the undoped samples, whereas for the doped samples, the conductivity continued to decrease when the incident photon energy increased to 3.06 eV. Despite the actual applied voltage during the *I–V* curve measurement reaching a high value of 100 V, no signs of ion migration or secondary phase formation were observed after the measurement (Fig. S7). Therefore, the conductivity response must be attributed to the band structures of the samples, as has been previously reported for negative photoconductivity in two-dimensional materials caused by trap centers in the bandgap.[56]

Fig. 7c and d propose the band structures in undoped and doped $Co(OH)_2$, respectively, during the photoconductivity measurement. Under dark conditions, the isolated in-gap state, which is approximately 1.7 eV or 1.5 eV above the valence band top (according to Fig. S4, see the edges of the absorption tails), does not contribute to the total conductivity. The origin of this in-gap state is attributed either to a low amount of Co_3O_4 phase found detected by XRD or to an intrinsic isolated trap state. The total conductivity (σ_{total}) is defined by the dark conductivity (σ_{dark}) and photoconductivity (σ_{photo}) *via* eqn (3):

$$\sigma_{total} = \sigma_{dark} + \sigma_{photo} = q(n_e + \Delta n_e)\mu_e + q(n_h + \Delta n_h)\mu_h \quad (3)$$

where q is the elemental charge, n_e is the density of intrinsic free electrons, n_h is the density of intrinsic free holes, Δn_e is the density of photo-excited electrons, Δn_h is the density of photo-excited holes, and μ_e and μ_h are the mobilities of electrons

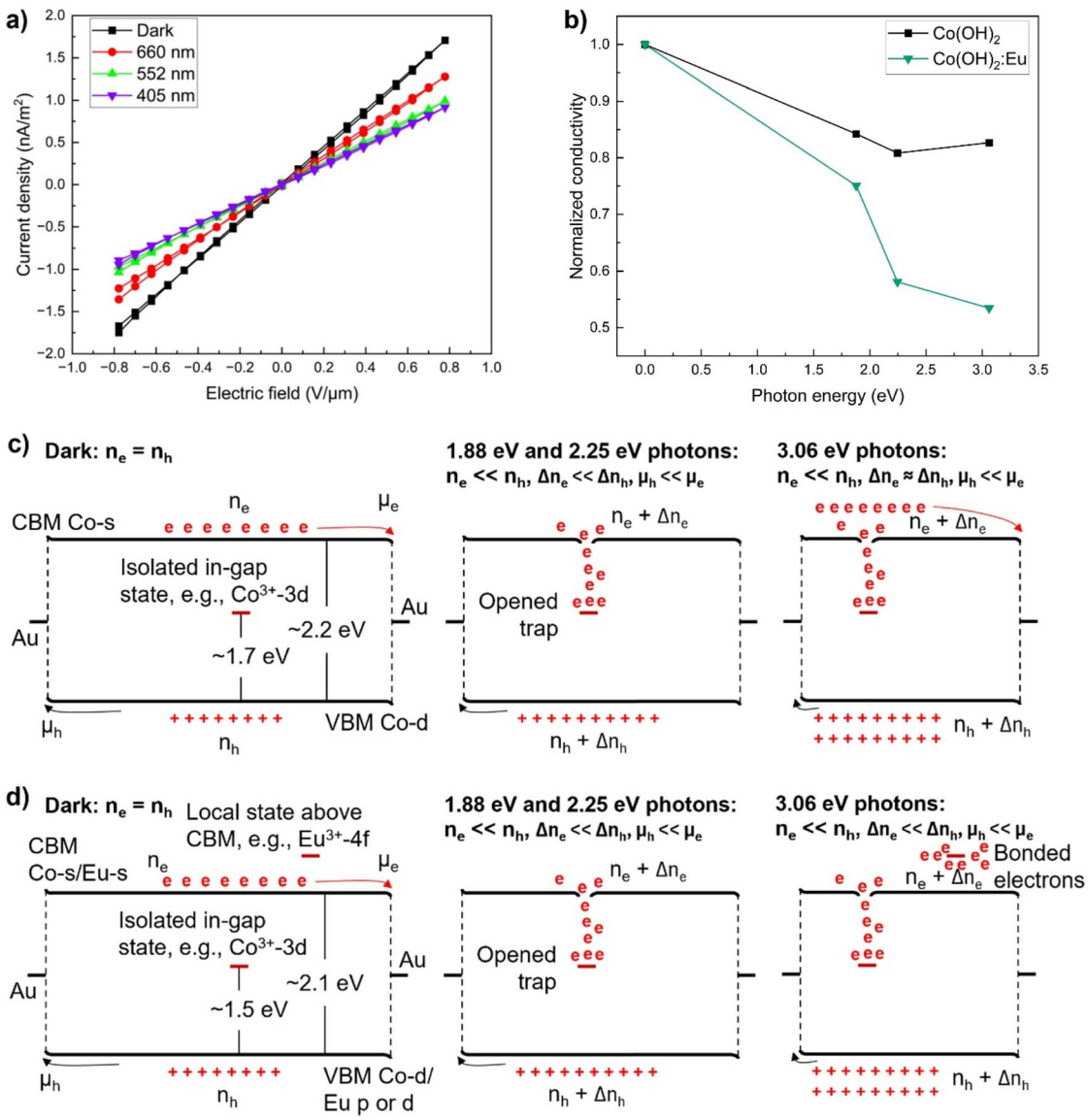

Fig. 7 Dependence of current density on electric field for a $Co(OH)_2$:Eu sample (a); dependence of normalized conductivity on photon energy for $Co(OH)_2$ and $Co(OH)_2$:Eu (b), where 0 eV represents the dark condition; schematic illustrations of band structures under photoconductivity measurement for $Co(OH)_2$ (c) and $Co(OH)_2$:Eu (d). CBM and VBM represent the conduction band bottom (minimum) and the valence band top (maximum), respectively.

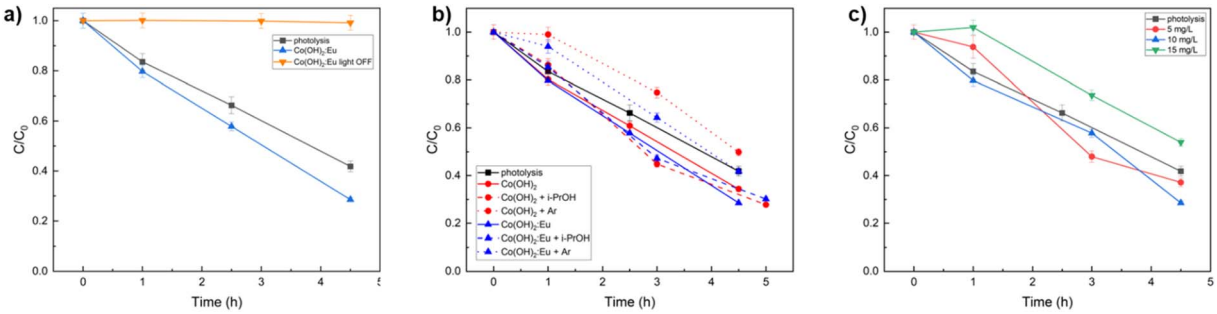

Fig. 8 Photocatalytic degradation of MB using $Co(OH)_2$:Eu ($n = 3$): comparison of $Co(OH)_2$:Eu for the photocatalytic degradation of MB under different conditions relative to photolysis (a), influence of radical scavengers (isopropanol and Ar atmosphere) on photocatalytic activity of $Co(OH)_2$ and $Co(OH)_2$:Eu (b), and photocatalytic degradation of different concentrations of MB by $Co(OH)_2$:Eu (c).

and holes, respectively. Therefore, under dark conditions, all intrinsic free electrons and holes contribute to the total conductivity, while no photo-excited charge carriers exist, that is, $\sigma_{total} = q(n_e\mu_e + n_h\mu_h)$. Upon illumination with a photon energy of 1.88 eV, the isolated gap state is opened as a charge trap. As a consequence, n_e significantly decreases and Δn_e is even negligible because most free electrons are localized in the trap. Although n_h may stay the same, because in semiconductors μ_h is usually much smaller than μ_e, the generation of Δn_h is not able to compensate for the loss of n_e and Δn_e that can migrate much faster. This leads to a decrease in σ_{total}. The situation stays similar under the photon energy of 2.25 eV, which is comparable to the band gap values. More electrons can be excited under 2.25 eV compared to the situation of 1.88 eV, and hence electrons have a larger probability to be localized. This causes σ_{total} to continue to decrease.

For undoped $Co(OH)_2$, no local state exists above the conduction band bottom. When the incident photon energy increases to 3.06 eV, Δn_e is largely recovered by the contribution of electrons that are excited to higher energy levels. Due to this, σ_{total} stops decreasing. On the other hand, the state above the conduction band bottom of the doped $Co(OH)_2$ may continue to localize the higher-energy excited electrons under photons of 3.06 eV, leading to a continuous decrease of σ_{total}. This characteristic offers the possibility of using undoped and europium-doped $Co(OH)_2$ as a pair for photodetection or photo-switching under violet or UV light, with the unfilled 4f states above the conduction band edge to influence it to the full extent.

Fig. S8a shows the chronoamperometry profiles of $Co(OH)_2$ and $Co(OH)_2$:Eu obtained at an applied potential of 0.3 V *vs.* Ag/AgCl. The photocurrent response is higher for the modified material, $Co(OH)_2$:Eu. The net photocurrent is affected by the light absorption, charge generation, separation, and surface kinetics. The smaller band gap of $Co(OH)_2$:Eu provides better visible light absorption and more photogenerated charges, which leads to a higher photocurrent response. From Mott–Schottky analysis (Fig. S8b), the flat band potential (F_b) and donor density (N_d) were obtained. These values are summarized in Table S4. The Mott–Schottky test served as additional confirmation that both materials possess the properties of n-type semiconductors, as demonstrated in Fig. 6b.

To further study the difference in the photoinduced processes upon Eu^{3+} doping, photocatalytic degradation of the methylene blue (MB) pigment was performed and compared with the degradation of the pigment under the same conditions without the doped $Co(OH)_2$ being present. Changes in the rate of MB degradation when using both undoped and europium-doped $Co(OH)_2$ are shown in Fig. 8a.

Higher degradation efficiency in the presence of $Co(OH)_2$:Eu (Fig. 8b) compared to photolysis proves the photocatalytic properties of the synthesized material. However, the efficiency of the degradation compared to undoped $Co(OH)_2$ is slightly better despite the EIS and photoluminescence results suggesting the opposite, which could confirm the presence of non-radiative recombination in pure $Co(OH)_2$. The adsorption properties of $Co(OH)_2$:Eu did not influence the experiment, as proven by the degradation experiment of methylene blue in the presence of the photocatalyst and in the absence of light irradiation.

The same degradation reaction also occurred when using other concentrations of methylene blue. As shown in Fig. 8c, the photocatalytic degradation of a 15 mg L^{-1} methylene blue solution followed a similar trend, even though at a lower rate, explained by exceeding the limit of the photocatalyst capabilities and covering of the active sites of the photocatalyst with dye molecules.[114] The photocatalytic degradation of the methylene blue solution, which was twice more diluted than the original solution studied (5 mg L^{-1}), followed a similar trend as well; however, the methylene blue determination proved to be more difficult as the absorption values were approaching the quantification limit.

Radical scavenger experiments were used to confirm the influence of $OH^{\bullet}$ radicals on the reaction (Fig. 8b) and to compare the mechanism using the undoped and doped $Co(OH)_2$. In Fig. S9a and b, it is demonstrated that upon addition of isopropanol, which acts as a scavenger of the hydroxyl radical, the degradation of methylene blue slows down already during the first hour of the experiment. Considering the band edge positions (valence band maximum 1.34 V *vs.* NHE), $Co(OH)_2$ will not be able to oxidize water to hydroxyl radicals directly (redox potential 2.80 V at pH 0),[115] which are demonstrated to be responsible for photocatalytic degradation. In this

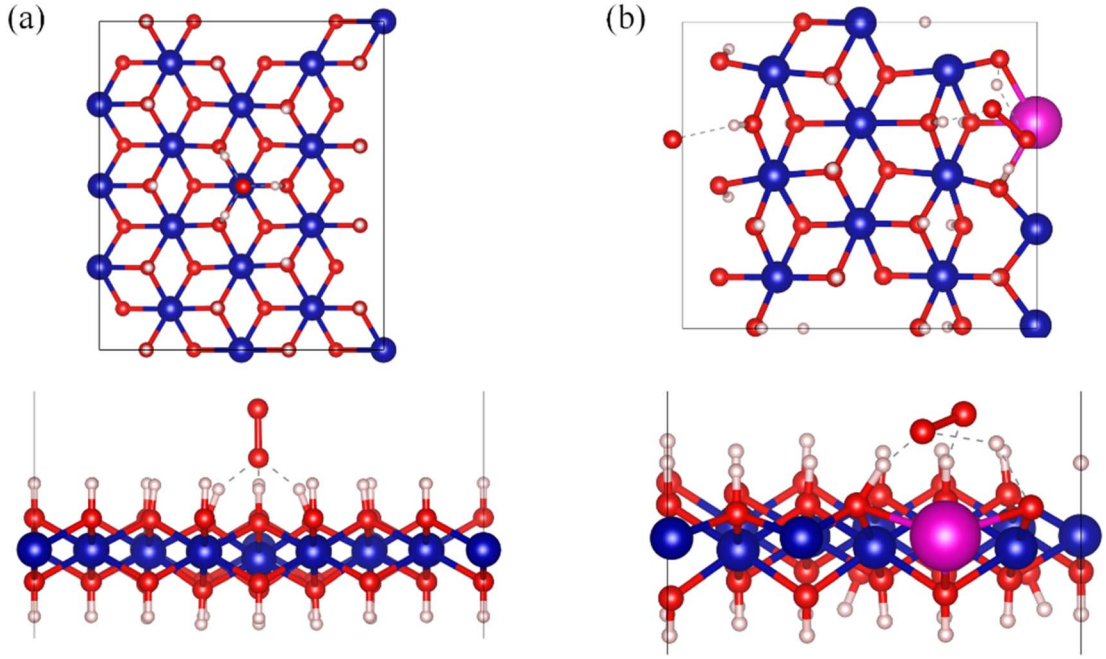

Fig. 9 Structural diagram of O_2 adsorption on $Co(OH)_2$ (a) and $Co(OH)_2$:Eu (b).

case, the $O_2^{-\bullet}$ radicals are formed at the valence band and are then converted to $OH^\bullet$ radicals in solution, as confirmed in previous studies.[30] As mentioned in Table S4, $Co(OH)_2$:Eu exhibits a more negative flat band potential, related to a stronger reducing power of electrons. Hence, it is more inclined to transform $O_2 \rightarrow O_2^{-\bullet} \rightarrow H_2O_2 \rightarrow OH^\bullet$, which are the main species involved in organic dye degradation. A higher N_d provides better electronic conductivity and carrier density. Therefore, even when R_{ct} is higher in this material, more charges reach the surface with a higher driving force, resulting in a higher photocurrent and photocatalytic organic dye degradation efficiency.

Experiments involving the scavenging of $O_2^{-\bullet}$ radicals were not conducted because the redox reaction between methylene blue and $K_2Cr_2O_7$, used to inhibit superoxide radical activity, interfered with the results. Instead, the methylene blue degradation reaction in an argon atmosphere was conducted and monitored (Fig. 8b). The anoxic atmosphere prevented the first step of oxygen adsorption on the surface of the photocatalyst, and, consequently, no superoxide radicals were formed, as confirmed by the decreased rate of methylene blue photocatalytic degradation.

The methylene blue photocatalytic degradation by $Co(OH)_2$:Eu was also checked in basic media (pH 9). As demonstrated by Fig. S9c, both photolysis and the photocatalytic reaction of methylene blue reached almost full degradation after an hour under light irradiation. At higher pH values, the cationic methylene blue molecule does not compete with H^+ for adsorption to the surface (negatively charged in basic solutions); thus, the subsequent degradation reaction occurs faster than at lower pH.[114,116–118] The higher stability of hydroxyl radicals and hydroxide ions at high pH values also increases the photocatalytic and photolysis rate. The photocatalytic degradation experiments were not performed in acidic media due to the instability of $Co(OH)_2$:Eu in acidic solutions.

DFT calculations helped us understand why the behaviours in photocatalytic degradation of doped and undoped samples were opposite to each other when compared to our expectations based on the photoluminescence and EIS results. Indeed, we could notice a higher degradation rate when using $Co(OH)_2$:Eu despite having an alleged higher recombination rate, as confirmed by photoluminescence and EIS. We ascribe this incongruence to a different capacity of the two materials to generate the designated radicals active in the degradation process. To explore the capacity of $Co(OH)_2$ to generate $O_2^{-\bullet}$ both before and after Eu doping, we initially constructed the structures of $Co(OH)_2$ adsorbing O_2 and $Co(OH)_2$:Eu adsorbing O_2, as depicted in Fig. 9. When $Co(OH)_2$ adsorbs O_2, the O atom is directly opposite to the Co atom, with the two O atoms vertically aligned. Conversely, when $Co(OH)_2$:Eu adsorbs O_2, the two O atoms are arranged diagonally, with one O atom positioned above the Eu atom. The O–O bond lengths are 1.38 Å and 1.40 Å, respectively, which differ from the O–O bond length of 1.21 Å in O_2 and are close to the O–O bond length of O_2^-, which is 1.33 Å.

To further validate that the optimized adsorbed species is $O_2^{-\bullet}$ rather than O_2, we calculated the differential charge density to ascertain the charge-transfer scenario. As presented in Fig. 10, the regions surrounding the oxygen atoms are yellow, denoting electron accumulation, while the outer regions are cyan, signifying electron depletion. This indicates that in both the cases of $Co(OH)_2$ and $Co(OH)_2$:Eu, electrons are transferred to O_2. To further quantify the charge transfer, Bader charge analyses were conducted. The results revealed that $Co(OH)_2$

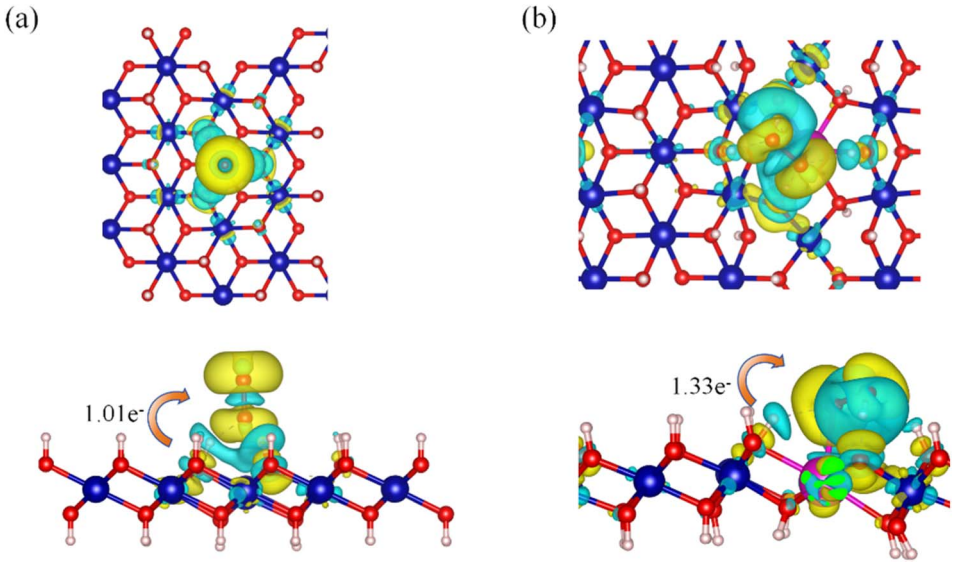

Fig. 10 Differential charge density of O_2 adsorption on $Co(OH)_2$ and $Co(OH)_2$:Eu, where yellow and cyan represent electron accumulation and depletion, respectively.

transferred 1.01|*e*| to O_2, and $Co(OH)_2$:Eu transferred 1.33|*e*| to O_2, further corroborating that both $Co(OH)_2$ and $Co(OH)_2$:Eu adsorb $O_2^{-\bullet}$. Additionally, when $Co(OH)_2$:Eu adsorbs O_2, Eu loses 1.43|*e*|, and Eu functions as an electron donor to facilitate the reduction of O_2 to $O_2^{-\bullet}$.

Furthermore, we calculated the adsorption energy (E_{ads}) using the formula $E_{ads} = E_{AB} - E_A - E_B$, where E_{AB} represents the total energy of O_2 adsorption on $Co(OH)_2$ (or $Co(OH)_2$:Eu), E_A refers to the energy of $Co(OH)_2$ (or $Co(OH)_2$:Eu), and E_B refers to the energy of O_2. The results indicate that the adsorption energy of O_2 on $Co(OH)_2$ is −3.89 eV, whereas that on $Co(OH)_2$:Eu is −11.37 eV. The more negative the adsorption energy, the more stable the adsorption. $Co(OH)_2$:Eu exhibits strong chemical adsorption of O_2, which can be stably immobilized on the surface. This provides ample time for electron transfer and prevents the premature desorption of O_2, which needs to be adsorbed in order to be reduced by the catalyst.

In summary, the adsorption energy of O_2 on $Co(OH)_2$:Eu (−11.37 eV) is markedly stronger than that on the undoped system (−3.89 eV). Moreover, the Bader charge analysis indicates that $Co(OH)_2$:Eu transfers 1.33|*e*| to O_2, which is close to the theoretical charge of the superoxide radical O_2^- (−1|*e*|). Although the undoped system can also generate $O_2^{-\bullet}$ (with a charge transfer of 1.01|*e*|), its weak adsorption leads to the facile desorption of O_2, resulting in lower actual catalytic efficiency due to a lower production of $OH^\bullet$ from $O_2^{-\bullet}$. The differential charge density further discloses that Eu doping significantly enhances the electron-supply capacity and the stability of $O_2^{-\bullet}$ by forming a Co–Eu synergistic electron transfer pathway, thereby more efficiently promoting the generation of superoxide radicals and the following production of $OH^\bullet$.

Radical scavenger experiments in combination with the DFT calculations of $O_2^{-\bullet}$ adsorption and desorption reveal that the key to more efficient photocatalytic properties of the doped system lies in the promotion of the superoxide radical and hence the hydroxyl radical production after irradiation with light. Despite the undoped hydroxide possessing ionic conductivity and a lack of radiative recombination, europium-doped cobalt hydroxide is still better suited to photocatalytic degradation as is proven on the basis of methylene blue degradation.

Conclusions

In this work, we have successfully synthesized europium-doped $Co(OH)_2$ nanoplates *via* a one-pot hydrothermal synthesis route for the first time. We have excluded the presence of bigger Eu-based aggregates and have confirmed the ions to be Eu^{3+}. More importantly, the comparative characterization has demonstrated a higher stability of $Co(OH)_2$:Eu for potentially increasing the time of use in photocatalysis, as is reflected by the increase in thermal stability by 30 °C. The photoconductivity studies showed that the introduction of trivalent europium ions into the crystal structure of cobalt hydroxide results in a 1.5-fold increase in the material's negative photoconductivity, offering the opportunity for further studies on rare-earth doped hydroxides in negative photoconductivity applications. Additionally, doping of $Co(OH)_2$ with trivalent europium ions increases the photocatalytic production of hydroxyl radicals, which are then actively used in degradation reactions, as demonstrated by the increase in methylene blue photocatalytic degradation from 66% to 72% compared to undoped $Co(OH)_2$. This work paves the way for the novel higher applicability of doped transition metal hydroxides in photo-mediated processes. Future studies may focus on the use of different dopants and/or hydroxides.

Author contributions

Viktorija Pankratova: investigation, formal analysis, visualization, writing – original draft, review & editing; Rossella Greco:

methodology, formal analysis, writing – review & editing; Takashi Yamamoto – investigation, formal analysis, writing – original draft; Joanna Hoszowska: writing – review & editing; Meng Zhang: investigation, formal analysis, writing – original draft; Ali M. Huerta-Flores: investigation, formal analysis, visualization, writing – review & editing; Miikka Willman: investigation, visualization; Kimmo Sirkka: investigation, writing – original draft; Vladimir Pankratov: investigation, writing – review & editing; Yang Bai: investigation, formal analysis, visualization, writing – review & editing; Wei Cao: funding acquisition, conceptualization, writing – review & editing.

Conflicts of interest

There are no conflicts to declare.

Data availability

The data reported here can be found on Zenodo at https://doi.org/10.5281/zenodo.17130017 or obtained upon reasonable request from the corresponding author.

Supplementary information (SI) is available. See DOI: https://doi.org/10.1039/d5ta07316b.

Acknowledgements

Viktorija Pankratova, Rossella Greco, and Wei Cao acknowledge funding from the European Research Council (ERC) under the European Union's Horizon 2020 Research and Innovation Programme (Grant Agreement No. 101002219). Kimmo Sirkka and Yang Bai acknowledge the funding from the European Union (ERC, UNIFY, 101039110). Ali M. Huerta-Flores acknowledges the University of Oulu & the Research Council of Finland Profi 352788, as well as the Nano and Molecular Systems Research Unit and the Sustainable Chemistry Unit for the acquisition of the Corrtest Instrument CS310M potentiostat and its consumables. The work has been partially supported by ERDF Project No. 1.1.1.3/1./24/A/077. Views and opinions expressed are, however, those of the authors only and do not necessarily reflect those of the European Union or the European Research Council. Neither the European Union nor the granting authority can be held responsible for them. The Center of Material Analysis (CMA), University of Oulu and Research Council of Finland (decision number 348700) are acknowledged. We acknowledge DESY (Hamburg, Germany), a member of the Helmholtz Association HGF, for the provision of experimental facilities. Parts of this research were carried out at Petra III. Data were collected using the P66 beamline Superlumi provided by DESY Photon Science. We would like to thank Dr Aleksei Kotlov for his assistance during the experiments. Beamtime was allocated for proposal I-20221411 EC. We are thankful to Dr Edgars Elsts (Institute of Solid State Physics, University of Latvia) for XRD measurements.

References

1 M. Grzegorzek, K. Wartalska and B. Kaźmierczak, *Int. Commun. Heat Mass Tran.*, 2023, **143**, 106674.
2 J. M. Quimbayo, S. Ojala, S. Urpelainen, M. Huuhtanen, W. Cao, M. Huttula and R. L. Keiski, *Advanced Oxidation Processes for Wastewater Treatment*, 2022, pp. 249–270.
3 S. Mishra, L. Acharya, B. Marandi, K. Sanjay and R. Acharya, *Diam. Relat. Mater.*, 2024, **142**, 110834.
4 L. Xie, J. G. Hao, H. Q. Chen, Z. X. Li, S. Y. Ge, Y. Mi, K. Yang and K. Q. Lu, *Catal. Commun.*, 2022, **162**, 106371.
5 C. Prasad, H. Tang, Q. Q. Liu, S. Zulfiqar, S. Shah and I. Bahadur, *J. Mol. Liq.*, 2019, **289**, 111114.
6 K. Maeda, K. Ishimaki, Y. Tokunaga, D. Lu and M. Eguchi, *Angew. Chem., Int. Ed.*, 2016, **55**, 8309–8313.
7 Z. Gao, Z. W. Yu, F. Q. Liu, C. Yang, Y. H. Yuan, Y. Yu and F. Luo, *ChemSusChem*, 2019, **12**, 4623–4628.
8 G. Liu, L. Wang, H. G. Yang, H. M. Cheng and G. Q. Lu, *J. Mater. Chem.*, 2010, **20**, 831–843.
9 R. Botella, W. Cao, J. Celis, J. Fernández-Catalá, R. Greco, L. Lu, V. Pankratova and F. Temerov, *J. Phys.: Condens. Matter*, 2024, **36**, 141501.
10 Z. You, D. Lu, K. K. Kondamareddy, W. Gu, Y. Su, J. Pan, J. Yang, P. Cheng and W. Ho, *Sep. Purif. Technol.*, 2025, **361**, 131293.
11 E. Kabir, P. Kumar, S. Kumar, A. A. Adelodun and K. H. Kim, *Renew. Sustain. Energy Rev.*, 2018, **82**, 894–900.
12 Z. Shan, Y. Yang, H. Shi, J. Zhu, X. Tan, Y. Luan, Z. Jiang, P. Wang and J. Qin, *Front. Chem.*, 2021, **9**, 755836.
13 J. Xiao, Y. Chen, C. Cai, S. Lai, L. Cheng, J. Zhang, W. Zhu, Y. Guo, M. Hou, L. Ma, W. Chen, X. Chen and C. P. Wong, *Small*, 2025, **21**, 2503335.
14 X. Xu, Z. Peng, H. Xu and D. Cheng, *J. Catal.*, 2022, **416**, 47–57.
15 B. Wang, J. Liu, S. Yao, F. Liu, Y. Li, J. He, Z. Lin, F. Huang, C. Liu and M. Wang, *J. Mater. Chem. A*, 2021, **9**, 17143–17172.
16 S. Ida and T. Ishihara, *J. Phys. Chem. Lett.*, 2014, **5**, 2533–2542.
17 R. Marschall and L. Wang, *Catal. Today*, 2014, **225**, 111–135.
18 F. M. Sanakousar, C. Vidyasagar, V. M. Jiménez-Pérez and K. Prakash, *Mater. Sci. Semicond. Process.*, 2022, **140**, 106390.
19 S. Samuei, S. S. Akbari, E. Ülker and F. Karadas, *Catal. Sci. Technol.*, 2022, **12**, 3044–3053.
20 L. Chen, H. Zhang, L. Chen, X. Wei, J. Shi and M. He, *J. Mater. Chem. A*, 2017, **5**, 22568–22575.
21 C. Wang, W. Li, A. A. Kistanov, H. Singh, Y. Kayser, W. Cao and B. Geng, *J. Colloid Interface Sci.*, 2022, **628**, 398–406.
22 B. Zheng, J. Fan, B. Chen, X. Qin, J. Wang, F. Wang, R. Deng and X. Liu, *Chem. Rev.*, 2022, **122**, 5519–5603.
23 Z. M. El-Bahy, A. A. Ismail and R. M. Mohamed, *J. Hazard. Mater.*, 2009, **166**, 138–143.
24 Y. Zhang, H. Zhang, Y. Xu and Y. Wang, *J. Solid State Chem.*, 2004, **177**, 3490–3498.

25 Z. Liang, Y. Zhang, G. Zhang, J. Liu, Y. Cai, Y. Wang, Y. Zhao, G. Li and K. Bei, *Int. J. Hydrogen Energy*, 2023, **48**, 18644–18656.
26 H. Liu, D. Wierzbicki, R. Debek, M. Motak, T. Grzybek, P. Da Costa and M. E. Gálvez, *Fuel*, 2016, **182**, 8–16.
27 P. Talebi, H. Singh, E. Rani, M. Huttula and W. Cao, *RSC Adv.*, 2021, **11**, 2733–2743.
28 P. Talebi, R. Greco, T. Yamamoto, M. Zeynali, S. Asgharizadeh and W. Cao, *Mater. Adv.*, 2024, **5**, 2968–2973.
29 R. Chen, H. Zhu, W. Liu, D. Zhan, Q. Fu, J. Tian, Y. Huang and C. Han, *J. Am. Ceram. Soc.*, 2024, **107**, 5201–5211.
30 R. Greco, L. Baxauli-Marin, F. Temerov, M. Daboczi, S. Eslava, Y. Niu, A. Zakharov, M. Zhang, T. Li and W. Cao, *Chem. Eng. J.*, 2023, **471**, 144569.
31 P. Bai, J. Xie, H. Wang, X. Kang and X. Wang, *Appl. Surf. Sci.*, 2023, **640**, 158305.
32 T. Y. Ma, S. Dai, M. Jaroniec and S. Z. Qiao, *J. Am. Chem. Soc.*, 2014, **136**, 13925–13931.
33 H. Li, C. Sun, Y. Zhao, X. Xu and H. Yu, *J. Nanopart. Res.*, 2018, **20**, 1–13.
34 X. Ma, Y. Liu, Y. Wang and Z. Jin, *Int. J. Hydrogen Energy*, 2021, **46**, 33809–33822.
35 C. Gao, Q. Meng, K. Zhao, H. Yin, D. Wang, J. Guo, S. Zhao, L. Chang, M. He, Q. Li, H. Zhao, X. Huang, Y. Gao and Z. Tang, *Adv. Mater.*, 2016, **28**, 6485–6490.
36 J. Fernández-Catalá, L. Jussila, M. Daboczi, F. Temerov, S. Eslava, R. Greco and W. Cao, *Cryst. Growth Des.*, 2023, **23**, 8828–8837.
37 J. Fernández-Català, J. Chávez-Caiza, R. Greco, M. Navlani-García, A. Berenguer-Murcia, W. Cao and D. Cazorla-Amorós, *Inorg. Chem. Commun.*, 2025, **178**, 114424.
38 G. Sorekine, G. Anduwan, M. N. Waimbo, H. Osora, S. Velusamy, S. Kim, Y. S. Kim and J. Charles, *J. Mol. Struct.*, 2022, **1248**, 131487.
39 M. Gunawan, M. Priest, D. Gunawan, S. Nie, A. Satriyatama, J. Vongsvivut, Z. Hameiri, Q. Zhang, S. Zhou and R. Amal, *Energy Environ. Sustain.*, 2025, **1**, 100019.
40 R. Greco, J. Fernandez-Catalá, J. Quimbayo and R. Botella, *Advanced Energy and Sustainability Research*, 2025, p. 2500123.
41 K. G. M. Laurier, F. Vermoortele, R. Ameloot, D. E. De Vos, J. Hofkens and M. B. J. Roeffaers, *J. Am. Chem. Soc.*, 2013, **135**, 14488–14491.
42 G. Jayanthi, S. Sumathi, K. Kannan, V. Andal and S. Murugan, *Adv. Mater. Sci. Eng.*, 2022, 6607683.
43 M. Gao, W. Sheng, Z. Zhuang, Q. Fang, S. Gu, J. Jiang and Y. Yan, *J. Am. Chem. Soc.*, 2014, **136**, 7077–7084.
44 S. Anantharaj, K. Karthick and S. Kundu, *Mater. Today Energy*, 2017, **6**, 1–26.
45 H. Wang, B. Shao, Y. Chi, S. Lv, C. Wang, B. Li, H. Li, Y. Li and X. Yang, *Nanomaterials*, 2022, **12**, 946.
46 L. Mao, Q. Ba, X. Jia, S. Liu, H. Liu, J. Zhang, X. Li and W. Chen, *RSC Adv.*, 2019, **9**, 1260–1269.
47 Y. Li, Y. Hou, Q. Fu, S. Peng and Y. H. Hu, *Appl. Catal., B*, 2017, **206**, 726–733.
48 Y. Zhang, Z. Jin, X. Yan, H. Wang and G. Wang, *Catal. Lett.*, 2019, **149**, 1174–1185.
49 Y. Zhan, G. Du, S. Yang, C. Xu, M. Lu, Z. Liu and J. Y. Lee, *ACS Appl. Mater. Interfaces*, 2015, **7**, 12930–12936.
50 L. Huang, J. Jiang and L. Ai, *ACS Appl. Mater. Interfaces*, 2017, **9**, 7059–7067.
51 G. Zhang, S. Zang and X. Wang, *ACS Catal.*, 2015, **5**, 941–947.
52 L. J. Zhang, R. Zheng, S. Li, B. K. Liu, D. J. Wang, L. L. Wang and T. F. Xie, *ACS Appl. Mater. Interfaces*, 2014, **6**, 13406–13412.
53 S. Liu, R. T. Gao, M. Sun, Y. Wang, T. Nakajima, X. Liu, W. Zhang and L. Wang, *Appl. Catal., B*, 2021, **292**, 120063.
54 Y. Zhao, X. Jia, G. I. N. Waterhouse, L. Z. Wu, C. H. Tung, D. O'Hare and T. Zhang, *Adv. Energy Mater.*, 2016, **6**, 1501974.
55 M. Suksomboon, K. Kongsawatvoragul, S. Duangdangchote and M. Sawangphruk, *ACS Omega*, 2021, **6**, 20804–20811.
56 B. Cui, Y. Xing, J. Han, W. Lv, W. Lv, T. Lei, Y. Zhang, H. Ma, Z. Zeng and B. Zhang, *Chin. Phys. B*, 2021, **30**, 028507.
57 N. K. Tailor, C. A. Aranda, M. Saliba and S. Satapathi, *ACS Mater. Lett.*, 2022, **4**, 2298–2320.
58 M. Y. Hassan and D. S. Ang, *ACS Appl. Mater. Interfaces*, 2019, 42339–42348.
59 S. Rahman, S. Samanta, A. Kuzmin, D. Errandonea, H. Saqib, D. L. Brewe, J. Kim, J. Lu and L. Wang, *Adv. Sci.*, 2019, **6**, 1901132.
60 B. Sreelakshmi and R. Thamankar, *Mater. Adv.*, 2024, **5**, 5912–5921.
61 B. Schwenzer, J. R. Neilson, K. Sivula, C. Woo, J. M. J. Fréchet and D. E. Morse, *Thin Solid Films*, 2009, **517**, 5722–5727.
62 K. Chatterjee, A. Dutta, S. Mishra, B. Bairy, M. B. Sen, A. Gorai, S. K. Saha and A. J. Akhtar, *Ceram. Int.*, 2023, **49**, 32768–32778.
63 U. Basak, P. Ghosh, D. P. Chatterjee, G. Mahapatra, A. Banerjee and A. K. Nandi, *J. Mater. Chem. A*, 2025, **13**, 7813–7833.
64 A. A. Minnekhanov, N. T. Le, E. A. Konstantinova and P. K. Kashkarov, *Appl. Magn. Reson.*, 2017, **48**, 335–345.
65 D. Nečas and P. Klapetek, *Cent. Eur. J. Phys.*, 2012, **10**, 181–188.
66 T. Taguchi, J. Harada, A. Kiku, K. Tohji and K. Shinoda, *J. Synchrotron Radiat.*, 2001, **8**, 363–365.
67 T. Taguchi, T. Ozawa and H. Yashiro, *Phys. Scr., T*, 2005, **115**, 205–206.
68 A. L. Ankudinov, B. Ravel, J. J. Rehr and S. D. Conradson, *Phys. Rev. B:Condens. Matter Mater. Phys.*, 1998, **58**, 7565.
69 V. Pankratov and A. Kotlov, *Nucl. Instrum. Methods Phys. Res., Sect. B*, 2020, **474**, 35–40.
70 Y. Smortsova, O. Chukova, M. Kirm, V. Nagirnyi, V. Pankratov, A. Kataev and A. Kotlov, *J. Synchrotron Radiat.*, 2025, **32**, 1539–1548.
71 X. Chen, S. Shen, L. Guo and S. S. Mao, *Chem. Rev.*, 2010, **110**, 6503–6570.
72 G. Kresse and J. Furthmüller, *Phys. Rev. B:Condens. Matter Mater. Phys.*, 1996, **54**, 11169.

73 J. P. Perdew, K. Burke and M. Ernzerhof, *Phys. Rev. Lett.*, 1996, **77**, 3865.
74 J. A. White and D. M. Bird, *Phys. Rev. B:Condens. Matter Mater. Phys.*, 1994, **50**, 4954.
75 H. J. Monkhorst and J. D. Pack, *Phys. Rev. B*, 1976, **13**, 5188.
76 S. Grimme, J. Antony, S. Ehrlich and H. Krieg, *J. Chem. Phys.*, 2010, **132**, 43.
77 J. Feng and H. C. Zeng, *Chem. Mater.*, 2003, **15**, 2829–2835.
78 Z. P. Xu and H. C. Zeng, *J. Mater. Chem.*, 1998, **8**, 2499–2506.
79 H. Ebrahimzade, G. R. Khayati and M. Schaffie, *Adv. Powder Technol.*, 2017, **28**, 2779–2786.
80 J. Yang, H. Liu, W. N. Martens and R. L. Frost, *J. Phys. Chem. C*, 2010, **114**, 111–119.
81 E. Higuchi, H. Otsuka, M. Chiku and H. Inoue, *J. Power Sources*, 2014, **248**, 762–768.
82 T. Baird, K. C. Campbell, P. J. Holliman, R. W. Hoyle, D. Stirling, B. P. Williams and M. Morris, *J. Mater. Chem.*, 1997, **7**, 319–330.
83 K. M. Cole, D. W. Kirk and S. J. Thorpe, *Surf. Sci. Spectra*, 2020, **27**, 024013.
84 J. P. Baltrus and M. J. Keller, *Surf. Sci. Spectra*, 2019, **26**(1), 014001.
85 M. C. Biesinger, B. P. Payne, A. P. Grosvenor, L. W. M. Lau, A. R. Gerson and R. S. C. Smart, *Appl. Surf. Sci.*, 2011, **257**, 2717–2730.
86 D. Hunt, G. Garbarino, J. Alberto Rodríguez-Velamazán, V. Ferrari, M. Jobbagy and D. A. Scherlis, *Phys. Chem. Chem. Phys.*, 2016, **18**, 30407–30414.
87 N. Di, J. Kubal, Z. Zeng, J. Greeley, F. Maroun and P. Allongue, *Appl. Phys. Lett.*, 2015, **106**, 122405.
88 Y. Zhang, T. Gao, F. Zhang, X. Qu, Y. Luo, P. Zhang, J. Liang, Y. Song, F. Fang, F. Wang, D. Sun and Y. Liu, *Adv. Energy Mater.*, 2024, **14**, 2401834.
89 M. N. Taran and G. R. Rossman, *Am. Mineral.*, 2001, **86**, 889–895.
90 N. V. Kosova, V. F. Anufrienko, T. V. Larina, A. Rougier, L. Aymard and J. M. Tarascon, *J. Solid State Chem.*, 2002, **165**, 56–64.
91 C. P. Roshni, K. Jithesh, P. M. Anjana, K. Govind Raj and R. B. Rakhi, *Next Mater.*, 2024, **4**, 100199.
92 M. Wang, J. Q. Wang, C. Xi, C. Q. Cheng, C. Q. Zou, R. Zhang, Y. M. Xie, Z. L. Guo, C. C. Tang, C. K. Dong, Y. J. Chen and X. W. Du, *Angew. Chem., Int. Ed.*, 2020, **59**, 11510–11515.
93 L. Wang, Z. Fang, T. Qi, L. Xing, J. Liu, S. Zhang, P. Xu and P. Ning, *J. Colloid Interface Sci.*, 2020, **571**, 90–99.
94 M. Nagli and M. Caspary Toroker, *Solid State Ionics*, 2018, **314**, 149–155.
95 J. Chen and A. Selloni, *J. Phys. Chem. C*, 2013, **117**, 20002–20006.
96 J. M. Ogiegło, A. Katelnikovas, A. Zych, T. Jüstel, A. Meijerink and C. R. Ronda, *J. Phys. Chem. A*, 2013, **117**, 2479–2484.
97 Y. Ou, W. Zhou, F. Ma, C. Liu, R. Zhou, F. Su, Y. Huang, P. Dorenbos and H. Liang, *J. Rare Earths*, 2020, **38**, 514–522.
98 F. T. Geldasa, M. A. Kebede, M. W. Shura and F. G. Hone, *AIP Adv.*, 2022, **12**, 115302.
99 D. H. Neuhaus, P. P. Altermatt, R. P. Starre, A. Schenk and A. G. Aberle, *Conference Record of the IEEE Photovoltaic Specialists Conference*, 2000, pp. 104–107.
100 S. Shionoya, W. M. Yen and H. Yamamoto, *Phosphor Handbook*, CRC Press, Boca Raton, 2nd edn, 2006.
101 M. Tabei, S. Shionoya and H. Ohmatsu, *Jpn. J. Appl. Phys.*, 1975, **14**, 240–247.
102 F. Baur and T. Jüstel, *Opt. Mater.:X*, 2019, **1**, 100015.
103 V. Serga, R. Burve, A. Krumina, V. Pankratova, A. I. Popov and V. Pankratov, *J. Mater. Res. Technol.*, 2021, **13**, 2350–2360.
104 Y. Liu, W. Luo, H. Zhu and X. Chen, *J. Lumin.*, 2011, **131**, 415–422.
105 Ž. Antić, R. M. Krsmanović, M. G. Nikolić, M. Marinović-Cincović, M. Mitrić, S. Polizzi and M. D. Dramićanin, *Mater. Chem. Phys.*, 2012, **135**, 1064–1069.
106 D. Sofich, S. G. Dorzhieva, O. D. Chimitova, B. G. Bazarov, Y. L. Tushinova, Z. G. Bazarova and R. Y. Shendrik, *Phys. Solid State*, 2019, **61**, 844–846.
107 A. Kuzmanoski, V. Pankratov and C. Feldmann, *Solid State Sci.*, 2015, **41**, 56–62.
108 R. Skaudzius, A. Katelnikovas, D. Enseling, A. Kareiva and T. Jüstel, *J. Lumin.*, 2014, **147**, 290–294.
109 L. Shirmane, C. Feldmann and V. Pankratov, *Phys. B*, 2017, **504**, 80–85.
110 P. Dorenbos, *J. Lumin.*, 2004, **108**, 301–305.
111 P. Dorenbos, *J. Phys.: Condens. Matter*, 2003, **15**, 8417.
112 S. Talukdar and R. K. Dutta, *RSC Adv.*, 2015, **6**, 928–936.
113 G. Cohen and R. E. Heikkila, *J. Biol. Chem.*, 1974, **249**, 2447–2452.
114 I. Khan, K. Saeed, I. Zekker, B. Zhang, A. H. Hendi, A. Ahmad, S. Ahmad, N. Zada, H. Ahmad, L. A. Shah, T. Shah and I. Khan, *Water*, 2022, **14**, 242.
115 Y. Deng and R. Zhao, *Curr. Pollut. Rep.*, 2015, **1**, 167–176.
116 T. N. T. Thu, N. N. Thi, V. T. Quang, K. N. Hong, T. N. Minh and N. L. T. Hoai, *J. Exp. Nanosci.*, 2016, **11**, 226–238.
117 N. R. Hendekhale and A. Mohammad-Khah, *J. Environ. Chem. Eng.*, 2020, **8**, 104065.
118 R. Hejazi, A. R. Mahjoub, A. H. C. Khavar and Z. Khazaee, *J. Photochem. Photobiol., A*, 2020, **400**, 112644.

